


Structure and Properties of Ti–Zr–Ni–Co–Cu High-Entropy Alloy After Powder Bed Fusion of Powders Produced by Mechanical Alloying and Plasma Spheroidization

N. G. Razumov¹ · T. Yu. Makhmutov¹ · A. Kim¹ · I. S. Goncharov² ·
N. E. Ozerskoi¹ · A. O. Silin¹ · E. V. Borisov¹ · K. A. Starikov¹ ·
A. K. Mazeeva¹  · A. A. Popovich¹

Received: 23 December 2021 / Accepted: 16 April 2022 / Published online: 20 May 2022
© The Indian Institute of Metals - IIM 2022

Abstract In this paper, the $\text{Ti}_{25}\text{Zr}_{25}\text{Ni}_{25}\text{Co}_{10}\text{Cu}_{15}$ high entropy alloy has been investigated. A novel approach to manufacture high-temperature shape memory alloys is proposed. A fundamental possibility to obtain compact samples by powder bed fusion using a laser beam (PBF-LB) from $\text{Ti}_{25}\text{Zr}_{25}\text{Ni}_{25}\text{Co}_{10}\text{Cu}_{15}$ powder obtained by mechanical alloying and plasma spheroidization is shown. During PBF-LB, a mixed structure is formed. It consists of B2-TiNi-type austenite with Laves phases and zirconium oxides. The average grain size is around 5 μm . The hardness of the alloy produced is more than 600 HV and significantly exceeds that of the alloy produced by conventional techniques. The ultimate compressive strength and the compressive yield strength of the samples are 640 MPa, and 600 MPa, respectively, meaning the synthesized samples are significantly inferior to the alloys produced by conventional smelting technologies. However, the ductility of 1.3% is comparable to that of similar alloys and indicates potential prospects of PBF-LB to manufacture Ti–Zr–Ni–Co–Cu HEAs.

Keywords High-entropy alloy · Mechanical alloying · Plasma spheroidization · Powder bed fusion using a laser beam · Additive manufacturing

1 Introduction

Nowadays, there is a tendency to design multi-component alloys with an almost equiatomic ratio of elements without an explicit base that leads to increase in the alloy's total entropy [1–3]. HEAs have proved to be alloys of high strength, wear, and corrosion resistance [3, 4].

However, their potential application is not limited to structural applications. Researchers currently show an interest in the functional properties of HEAs, in particular, in the shape memory effect (SME) [5]. A conventional, well-studied, and practically used shape memory alloy (SMA) is titanium nickelide TiNi. In papers [6–8], the authors took it as a base to design Ti–Zr–Hf–Ni–Co–Cu HEA with SME. In this composition, Zr and Hf make a substitutional solid solution with Ti, and Co and Cu occupying Ni positions that results in the formation of pseudobinary intermetallic (TiZrHf)(NiCoCu)-type compounds' properties. However, implementation of the HEA conception and addition of refractory elements widens their working temperature range and improves mechanical and functional properties [9, 10]. High-temperature SMAs can be used to manufacture new generation of valves for nuclear reactors. Such valves will operate automatically due to changes in the temperature of working gases within the SME temperature range which is much higher than a room temperature.

The functional properties of the SMA are associated with B2 \leftrightarrow B19' martensitic transformation, which is observed in an extremely narrow range of valence electron concentrations (VEC) = 7.0–7.2 for Ti–Zr–Hf–Ni–Co–Cu alloys [11]. According to analysis of papers [6–8], to obtain a high-temperature SME, the $(\text{TiZrHf})_{50}\text{Ni}_{25}\text{Co}_{10}\text{Cu}_{15}$ composition offers an advantage. However, the presence of

✉ A. K. Mazeeva
mazeevaalina@gmail.com

¹ Institute of Machinery, Materials and Transport, Peter the Great St. Petersburg Polytechnic University, Polytechnicheskaya, 29, Saint-Petersburg, Russian Federation 195251

² Department of Mechanical Engineering, Politecnico di Milano, Via Privata Giuseppe La Masa 1, 20156 Milan, Italy

Hf in the composition leads to a high probability of the formation of HfNi-type intermetallic compounds. It is caused by a decrease in the mixing entropy (ΔS (mix)) of the system, as well as the enthalpy contribution (ΔH (mix)) of Hf. Also, due to a decrease in the Ti content resulting from its partial replacement with Hf, the probability of precipitation of NiZr and Ni₁₁Zr₉-type intermetallic compounds also increases.

In papers [6–8], Ti–Zr–Hf–Ni–Co–Cu alloys were manufactured by arc melting; on several occasions, the ingot was subjected to subsequent rolling and heat treatment. As a result, it is possible to obtain only standard, quite simple product shapes such as rods, sheets, slabs which can no longer fully meet the growing demand for complex-shaped items in modern machinery.

One of the promising directions in the field of designing unique products of complex shapes is using additive 4D-technologies [12, 13]. They imply the use of additive manufacturing (AM) to create objects from smart materials, including SMAs [12].

The feedstock material for AM of metal products is usually a powder that must meet several stringent requirements. The main criteria are a high degree of sphericity and a relatively narrow fractional composition. In particular, for powder bed fusion using a laser beam (PBF-LB), the particle size should be in the range of 20–60 μm . At the moment, one of the most widespread methods to obtain spherical metal powders of various compositions is gas atomization [14]; however, it has several disadvantages, such as a high probability of gas porosity formation in the particles and the large number of satellites on the particles' surface [14].

In papers [15, 16], to obtain spherical metal powders, a combination of mechanical alloying (MA) and plasma spheroidization (PS) was proposed. This combination makes it possible to obtain metal powders with a wide range of chemical compositions. In addition, at the MA stage, the alloy's synthesis occurs without a melting process, which is especially important for the synthesis of refractory alloys. Plasma spheroidization allows the production of non-porous powders with a high yield of perfectly spherical particles.

Despite many papers devoted to manufacturing binary TiNi by AM [13, 17] and producing feedstock powders [18, 19], the direction of high-entropy SMAs produced by AM has not been studied in-depth.

This work aims to study the full production cycle of high-entropy shape memory Ti–Zr–Co–Ni–Cu alloy by PBF-LB with preliminary production of spherical powders by a combination of MA of elemental powders and subsequent PS and to analyze the effect of each technological stage on the HEA chemical composition, structure, and mechanical properties.

2 Materials and Methods

Optimal compositions were calculated by the CALPHAD method using Thermo-Calc software and the TCHEA4 database according to the criteria described in the Introduction section.

Due to this reason, the Hf-free Ti₂₅Zr₂₅Ni₂₅Co₁₀Cu₁₅ alloy was chosen for the research. The powder of this alloy was synthesized by MA followed by PS.

Elemental powders of Ti (purity 99.5%, particle size 100–150 μm), Zr (purity 99.0%, average particle size 10 μm), Ni (purity 99.5%, particle size 71–250 μm), Co (purity 99.5%, particle size 100–150 μm), Cu (purity 99.5%, particle size up to 100 μm) were used as feedstock materials.

Mechanical alloying was carried out by using a Fritsch Pulverisette 4 (Germany) vario-planetary mill in a high-purity argon atmosphere. High-strength steel balls with diameter of 7–10 mm were used for MA. The ratio of the mass of the milled material to the mass of the milling balls was 1:20, the rotation speed of the planetary disk/bowl was 200–400 rpm. The milling time was 5–15 h.

Plasma spheroidization was carried out by using a Tek-15 unit (Tekna Plasma Systems Inc.). The process parameters were as follows: plasma unit power, 15 kW; powder feed rate, 38 g/min. The plasma-forming gas was an argon–hydrogen mixture, consumed at rates of 50 l/min (Ar) and 3.5 l/min (H₂). The feed rate point was 0 mm (in the center of the induction coil).

Powder bed fusion using a laser beam was carried out using an SLM Solutions SLM 280 3D printer. The technological parameters are shown in Table 1. As a result, the values of the volume energy density (VED) calculated according to Eq. (1) are in the range of 120–154 J/mm³.

$$E_v = \frac{P}{v \cdot h \cdot t} \quad (1)$$

P —laser power, V —scanning speed, h —hatch distance, t —layer thickness.

MV1 double mode differs from MV1 mode by repeated laser scanning of each layer using MV1 mode parameters. After PBF-LB, the samples were annealed at 1050 °C in argon for 5.5 h with subsequent water quenching.

The phase composition was determined by X-ray diffraction (XRD) analysis by using a Bruker D8 Advance X-ray diffractometer with Cu-K α radiation ($\lambda = 0.15418$ nm). Further processing of the diffraction data was carried out according to the Rietveld method using the BRUKER Diffrac Plus Topas program. The study of structure, chemical composition, and distribution of elements was carried out by using a Tescan Mira 3 LMU scanning electron microscope equipped with an attachment for energy-dispersive spectral analysis. PBF-LB samples'

Table 1 Powder bed fusion using a laser beam modes

PBF-LB mode	P , W	V , mm/s	h , mm	Number of repeats	E_v , J/mm ³
<i>MV1</i>					
Contour	350	800	0.06	3	145
“Body”	288	800	0.06	1	120
<i>MV2</i>					
Contour	350	800	0.06	3	145
“Body”	370	1000	0.06	1	123
<i>MV3</i>					
Contour	370	800	0.06	3	154
“Body”	288	1000	0.06	1	123
<i>MV1 double</i>					
Contour	350	800	0.06	3	145
“Body”	288	800	0.06	2	120

porosity was determined by using Leica DIM5000 optical microscope equipped with Thixomet Pro software. The hardness of the samples was determined by the standard method according to the Vickers scale.

3 Results

Figures 1 and 2 show the element distribution maps of the powder particles after 5 and 15 h of MA. Mechanical alloying of the elemental powder occurs according to similar mechanisms described in [20]. It has been found that the confidence interval of the deviation from the average composition in the powder particles with a

confidence probability of 95% can reach 30% after 5 h of MA, indicating significant inhomogeneity in the chemical composition of individual powder particles. An increase in MA duration leads to a decrease in this parameter to the values of 1–3% indicating general homogenization. However, the difference between 10 and 15 h is insignificant, and the further MA seems inappropriate.

Intense mechanical impact during MA leads to distortions in the crystal lattice, induction of a high concentration of defects, and complete dissolution of elements (Fig. 3).

The following PS results in a powder made up of over 95% spheroidized particles. More than 85% of the particles have a spherical shape. Less than 5% of the particles have

Fig. 1 Element distribution in $Ti_{25}Zr_{25}Ni_{25}Co_{10}Cu_{15}$ powder particles after MA for 5 h: **a** general view; **b** Ti; **c** Zr; **d** Ni; **e** Co; **f** Cu

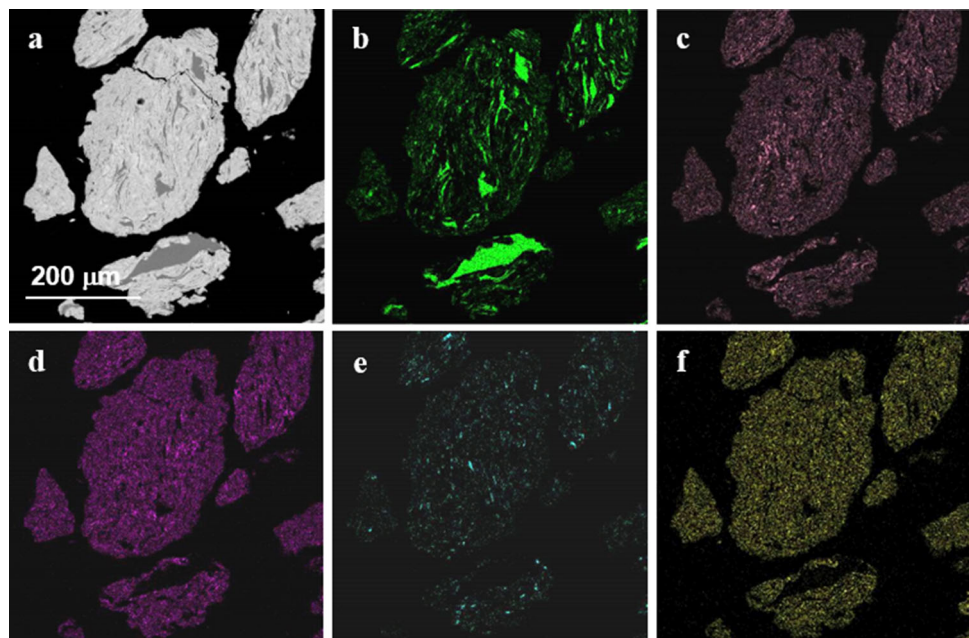


Fig. 2 Element distribution in $\text{Ti}_{25}\text{Zr}_{25}\text{Ni}_{25}\text{Co}_{10}\text{Cu}_{15}$ powder particles after MA for 15 h: **a** general view; **b** Ti; **c** Zr; **d** Ni; **e** Co; **f** Cu

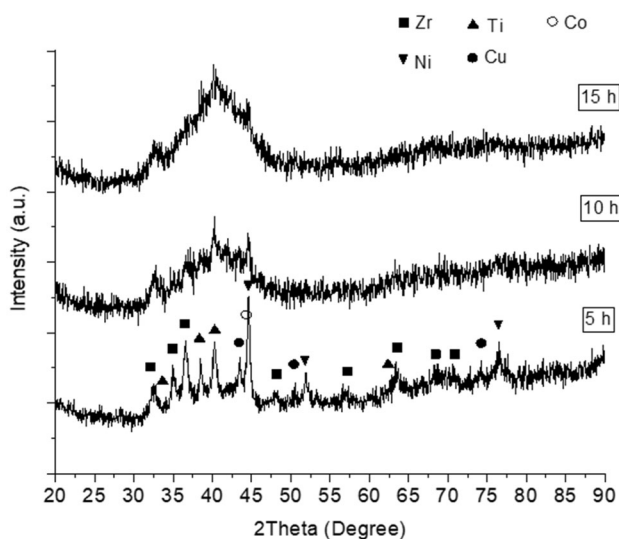
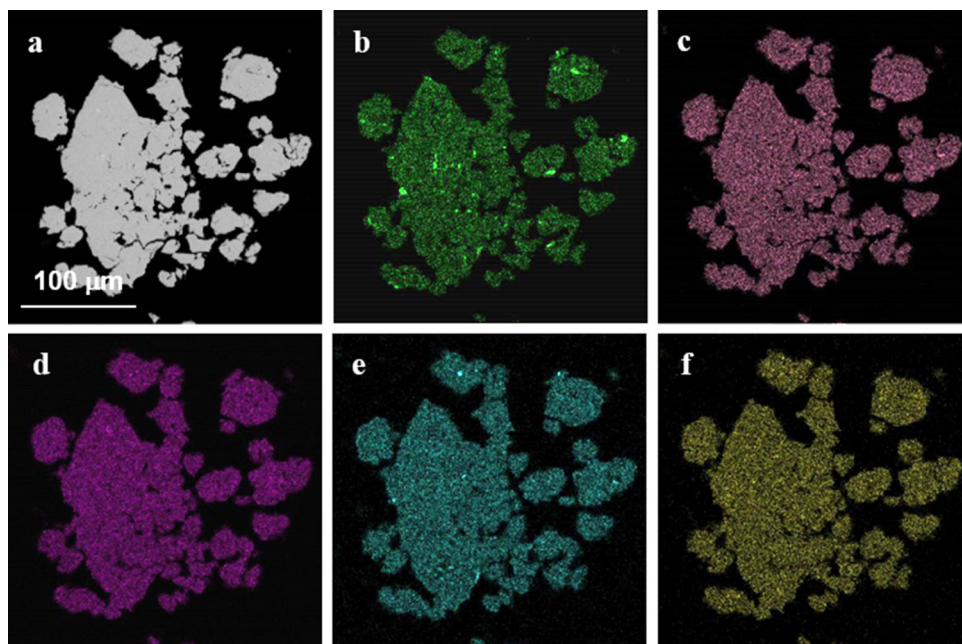


Fig. 3 Phase composition of $\text{Ti}_{25}\text{Zr}_{25}\text{Ni}_{25}\text{Co}_{10}\text{Cu}_{15}$ powder after MA in the planetary mill

an irregular shape; the rest have a rounded shape with the aspect ratio from 1.2 to 2.

Cross-sectional analysis of the $\text{Ti}_{25}\text{Zr}_{25}\text{Ni}_{25}\text{Co}_{10}\text{Cu}_{15}$ powder particles show a fine-grained structure with an average grain size of 2–3 μm (Fig. 4) and absence of porosity. The alloy contains three phases differing in contrast (gray, light gray, and dark gray). All three phases are based on a $(\text{TiZr})_x\text{Ni}_y$ -type intermetallic compound with a different stoichiometric ratio. When the molten particles leave the plasma torch and are cooled, they do not solidify immediately. Their solidification proceeds gradually from the surface to the center [14]. As a result, the

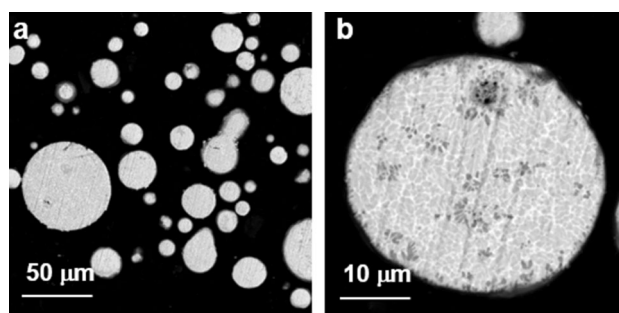


Fig. 4 The structure of $\text{Ti}_{25}\text{Zr}_{25}\text{Ni}_{25}\text{Co}_{10}\text{Cu}_{15}$ powder after plasma spheroidization: **a** $\times 1000$; **b** $\times 5000$

shell crystallizes very fast while the core remains liquid. The crystallization of the core is slowed down due to the shell crystallization's exothermic nature, resulting in the release of additional heat, which increases the temperature of the liquid inside the particle. As a result, secondary phases precipitate from the supersaturated solid solution in the core [14].

Analysis of the element distribution maps shows an increased Ni content in the light gray areas and Ti and Zr in the dark gray areas (Fig. 5). Unfortunately, the precipitations of the secondary phase are quite small, and in this case, the results of X-ray microanalysis are in a significant error. However, after collecting a sufficient amount of the measurement data, the following conclusion can be made: the dark gray component corresponds to the intermetallic compound with a low nickel content, $(\text{TiZr})_{1.8-2}\text{Ni}$; the primary, gray component, corresponds to the equiatomic compound $(\text{TiZr})_{0.9-1}\text{Ni}$, and the light gray component is enriched with nickel and has an approximate stoichiometry

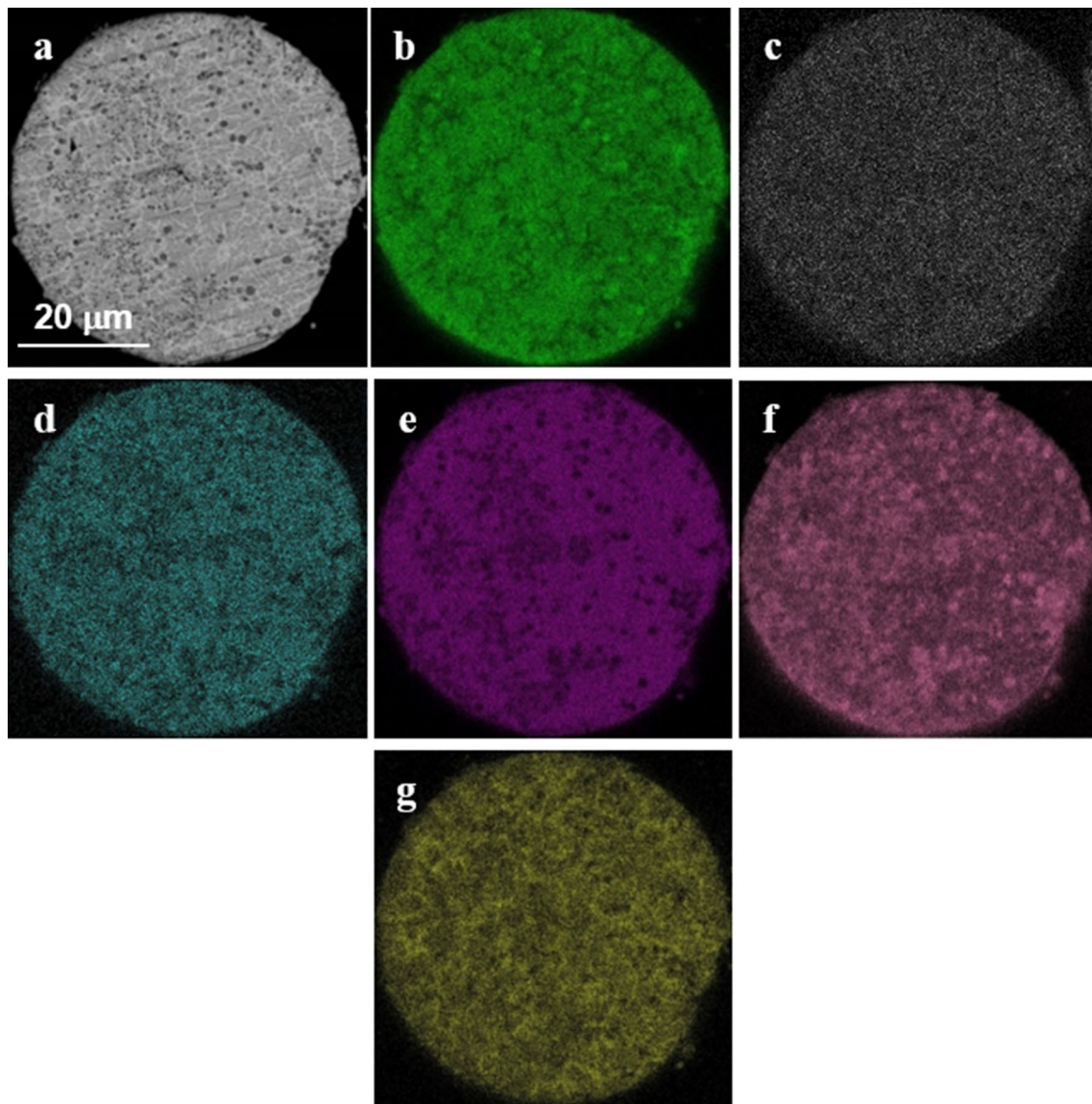


Fig. 5 Element distribution maps of $\text{Ti}_{25}\text{Zr}_{25}\text{Ni}_{25}\text{Co}_{10}\text{Cu}_{15}$ powder after plasma spheroidization: **a** general view; **b** Ti; **c** Fe; **d** Co; **e** Ni; **f** Zr; **g** Cu

$(\text{TiZr})_{0.7-0.75}\text{Ni}$. The results obtained are confirmed by XRD analysis (Fig. 6). The XRD pattern indicates the presence of two compounds with lattices corresponding to a B2-TiNi austenite and a NiZr_2 -type intermetallic compound. The B2-TiNi-type austenite phase has the lattice cell parameter $a = 3.015 \text{ \AA}$, which is close to the reference value ($a = 2.993 \text{ \AA}$ [21]). The second phase, $\text{Ti}(\text{Ni}_{0.5}\text{Cu}_{0.5})$, has a similar crystal structure but contains an additional substitutional atom. As a result, the lattice cell parameter increases and is $a = 3.041 \text{ \AA}$. In addition, there is an insufficient amount of compounds with a crystal structure corresponding to the B19'-NiTi- martensite, a NiZr_2 -type intermetallic compound, and zirconium oxide.

The results of the sample porosity measurements after PBF-LB are presented in Table 2. From the results, the dependence of the sample porosity on the VED values has been established. An increase in the VED negatively affects the porosity of the resulting product. The samples obtained at MV1 mode with the lowest VED value have a porosity of 0.5%. Repeated scanning of each layer according to MV1 mode leads to an increase in porosity by 25% (up to 0.63%). The use of modes with a higher VED increases porosity up to 1–1.5%.

The negative effect of high VED is explained by the formation of large melt pools, which increases the number of powder particles wetted and drawn into the melt. This

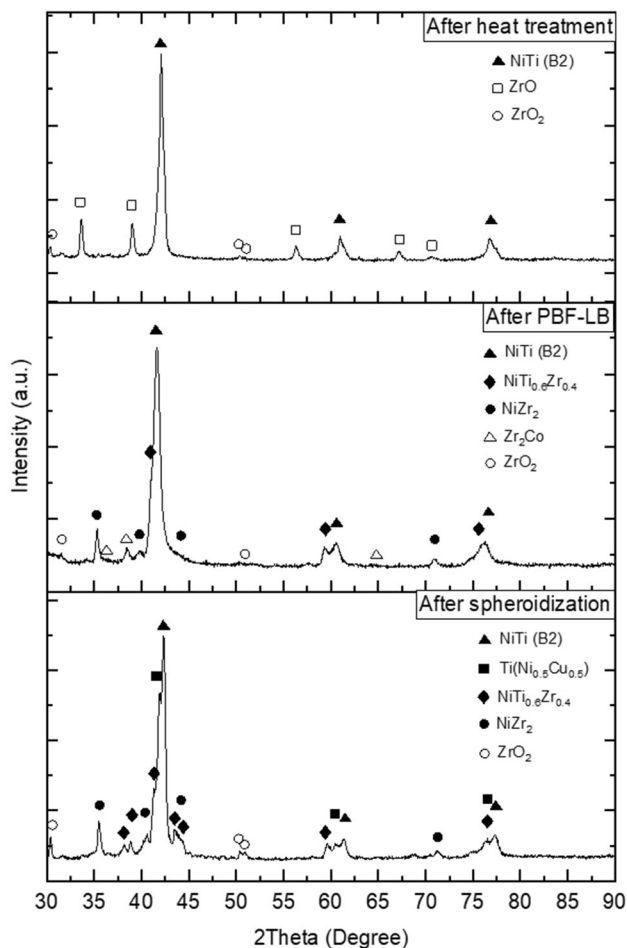


Fig. 6 Phase composition of the HEA powders after plasma spheroidization, PBF-LB process and subsequent heat treatment

Table 2 $Ti_{25}Zr_{25}Ni_{25}Co_{10}Cu_{15}$ porosity after PBF-LB

PBF-LB mode	Porosity, %
MV 1	0.50
MV 2	1.00
MV 3	1.53
MV 1 double	0.63

leads to distortions in the geometry of the surface layer and impedes the movement of the powder distributing blade.

Despite the lowest porosity value and the absence of visible defects after MV1 mode, this mode has been considered unsuitable for use since the samples are torn off from the substrate during the building process that can be caused by increased internal stresses at this mode. Double scanning at MV 1 double mode leads to some increase in the porosity; however, its values are rather low and does not lead to tearing-off of the sample from the substrate. Thus, the MV1 double mode is determined as the optimal

PBF-LB mode to obtain compact samples from $Ti_{25}Zr_{25}Ni_{25}Co_{10}Cu_{15}$ powder.

Figure 7 shows the microstructure of $Ti_{25}Zr_{25}Ni_{25}Co_{10}Cu_{15}$ samples produced by PBF-LB at different modes. There are almost no pores in all samples, and the structure contains three components that differ in contrast. They are a gray matrix, a dark gray component with corresponding to B2-TiNi austenite with the average grain size of $\sim 5 \mu m$, and white Laves phase inclusions, which are confirmed by the results of XRD showing the presence of the main B2 phase and Laves phases and lines corresponding to zirconium oxides ZrO and ZrO₂ (Fig. 6).

Analysis of the element distribution over a MV1 double sample cross-section (Fig. 8) shows that the B2-phase is almost homogeneous; the dark gray structural components are enriched with Zr. The differences of the concentrations in the points in the matrix (gray) and the veins (dark gray inclusions) are small but sufficient to explain the bifurcation and asymmetry of the B2-phase lines in the XRD patterns (Fig. 6). In the dark gray component, the concentration of Zr (with a larger atomic radius) is higher, and the concentration of Ti (with a smaller atomic radius) is lower than in the gray matrix. Therefore, the XRD peaks obtained from the dark gray inclusions are shifted toward smaller angles than the peaks obtained from the matrix, and their intensity is systematically lower than the intensity of the matrix peaks due to their lower content in the sample. Hence, it follows that B2-austenite decomposes with the formation of two solid solutions with well-defined, close to the average values, lattice periods. The B2 lattice periods calculated from the singlet coordinates of each doublet for the same sample are identical within a relatively small error (3.0577–3.1127 Å).

The element distribution maps show the presence of oxygen consistent with the presence of zirconium oxides ZrO and ZrO₂ (Fig. 6). The presence of the oxides can be explained by the content of undesirable impurities in the feedstock materials and the absorption of oxygen during the alloy processing since titanium alloys are sensitive even to insignificant oxygen concentrations under a low vacuum.

Table 3 shows the average chemical composition after PBF-LB. According to the data obtained, the chemical composition almost coincides with the nominal composition of the powder obtained by MA and subsequent PS.

According to the mechanical test results of the samples obtained at MV1 double mode, the sample's ultimate compressive strength is 640 MPa, the yield point is 600 MPa, the ductility is 1.3%, and the hardness is 637 HV (Fig. 9). After water quenching, the ultimate compressive strength increases up to 710 MPa, the plasticity is 1.5%, and the hardness is 642 HV.

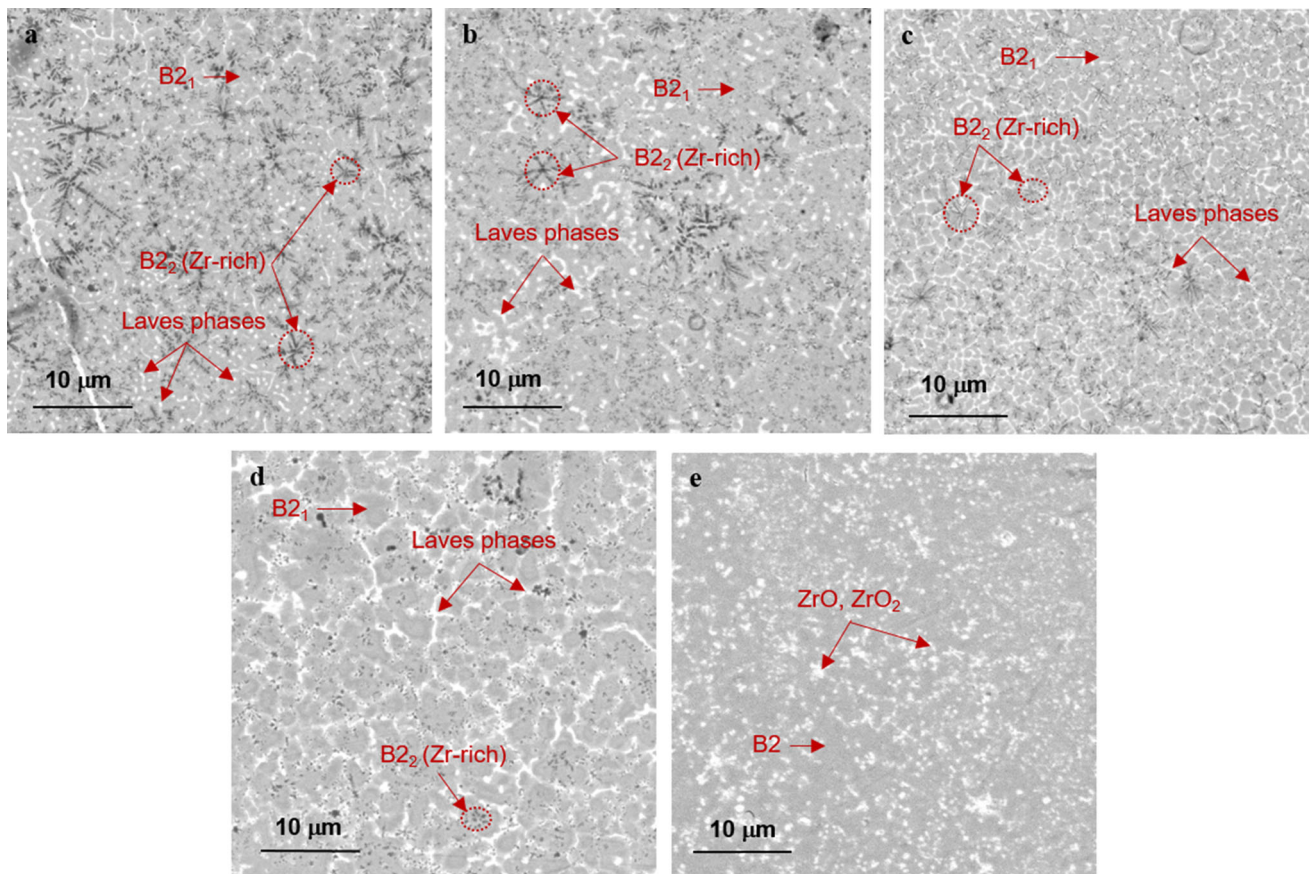


Fig. 7 SEM-images of $\text{Ti}_{25}\text{Zr}_{25}\text{Ni}_{25}\text{Cu}_{15}\text{Co}_{10}$ structure after PBF-LB at modes **a** MV1; **b** MV2; **c** MV3; **d** MV1 double; **e** MV1 double and subsequent heat treatment

4 Discussion

According to the mechanical test results, the samples' hardness, which is 630 HV and higher, is of the same order of magnitude as the hardness of this alloy obtained by arc melting [8]. This value significantly exceeds the hardness of any of the binary intermetallic compounds consisting of the HEA composition elements, which is no more than 280 HV. The increase in the hardness is achieved due to the implementation of the high-entropy alloy concept and by forming a crystal lattice with a high level of internal distortions. In addition, in practice, the structure of $\text{Ti}_{25}\text{Zr}_{25}\text{Ni}_{25}\text{Co}_{10}\text{Cu}_{15}$ alloy after PBF-LB contains secondary Laves C15 phases. A decrease in the Hf content in alloys of the Ti–Zr–Hf–Ni–Co–Cu system makes the alloys less prone to forming Laves phases; however, according to [8], even in Hf-free $\text{Ti}_{40}\text{Zr}_{10}\text{Ni}_{40}\text{Co}_5\text{Cu}_5$ alloy, there is about 1.7% of a C15 phase. Moreover, $\text{Ti}_{25}\text{Zr}_{25}\text{Ni}_{25}\text{Co}_{10}\text{Cu}_{15}$ HEA structure contains particles of zirconium oxides ZrO_2 , which, together with Laves phases, lead to precipitation hardening of the alloy.

In terms of compressive ultimate strength and compressive yield strength, the synthesized samples are

significantly inferior to the samples produced by conventional smelting technologies. In particular, in paper [8], for $\text{Ti}_{40}\text{Zr}_{10}\text{Ni}_{40}\text{Co}_5\text{Cu}_5$ and $\text{Ti}_{30}\text{Zr}_{20}\text{Ni}_{30}\text{Co}_{10}\text{Cu}_{10}$ alloys, the ultimate strength is 1940 and 1935 MPa, and the yield strength is 1070 and 1630 MPa, respectively.

The structure of the samples obtained at MV1 double mode contains a significant amount of Laves phase that is mainly located at the B2 grain boundaries (Fig. 7d) and leads to brittle fracture of the alloy at low compressive stress. Another reason for the low values of the yield and ultimate stresses is the porosity of the sample. Although it is rather low and indicated as 0.63%, it is sufficient to assist fracture at lower loads. Heating the samples to 1050 °C, followed by water quenching, makes it possible to obtain a more uniform B2 phase composition and partially dissolve precipitates in the matrix (Figs. 6 and 7e), but this does not lead to a significant change in the mechanical characteristics (Fig. 9). This fact can also be explained by the presence of Zr oxides that is most noticeable after water quenching (Fig. 6).

However, the ductility of the synthesized alloy, which is 1.3%, is comparable to that of $\text{Ti}_{30}\text{Zr}_{20}\text{Ni}_{30}\text{Co}_{10}\text{Cu}_{10}$ alloy,

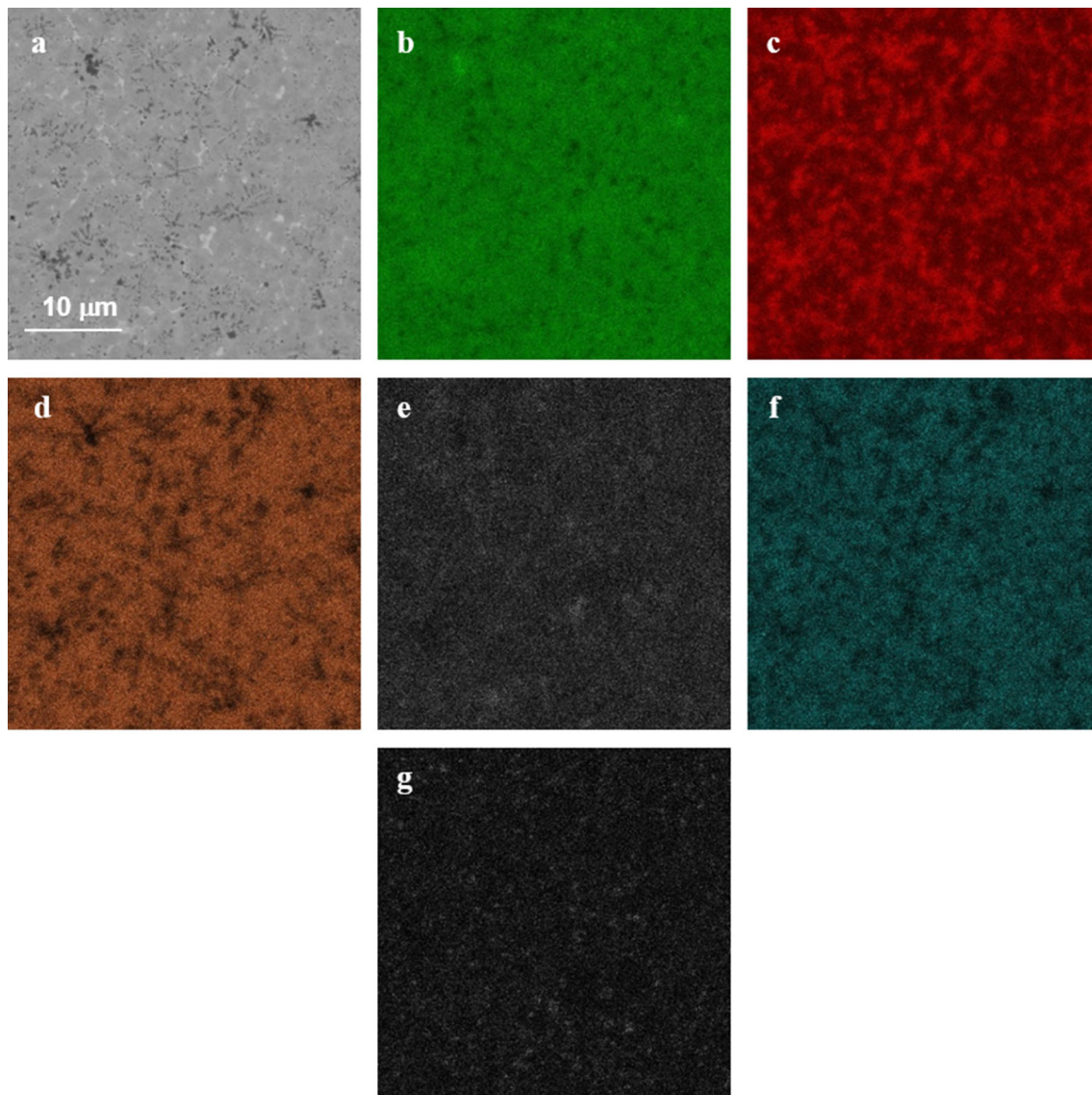


Fig. 8 Element distribution maps of $\text{Ti}_{25}\text{Zr}_{25}\text{Ni}_{25}\text{Cu}_{15}\text{Co}_{10}$ sample produced by PBF-LB at MV1 double mode **a** investigated area; **b** Ti; **c** Zr; **d** Ni; **e** Cu; **f** Co; **g** O

Table 3 Chemical compositions of $\text{Ti}_{25}\text{Zr}_{25}\text{Ni}_{25}\text{Cu}_{15}\text{Co}_{10}$ samples produced by PBF-LB, wt.%

Sample	Ti	Zr	Ni	Cu	Co	Fe
MV 1	37.30	16.59	33.99	5.31	5.47	1.34
MV 2	37.26	16.45	34.32	5.00	5.70	1.27
MV 3	36.58	16.05	34.65	5.69	5.64	1.40
MV 1 double	36.96	16.38	34.44	5.36	5.53	1.34

which is 1.8% [8], that indicates good prospects for using PBF-LB to obtain Ti–Zr–Ni–Co–Cu HEAs.

5 Conclusion

A fundamental possibility to obtain compact samples by powder bed fusion using a laser beam from $\text{Ti}_{25}\text{Zr}_{25}\text{Ni}_{25}\text{Co}_{10}\text{Cu}_{15}$ HEA powder synthesized by MA followed by PS

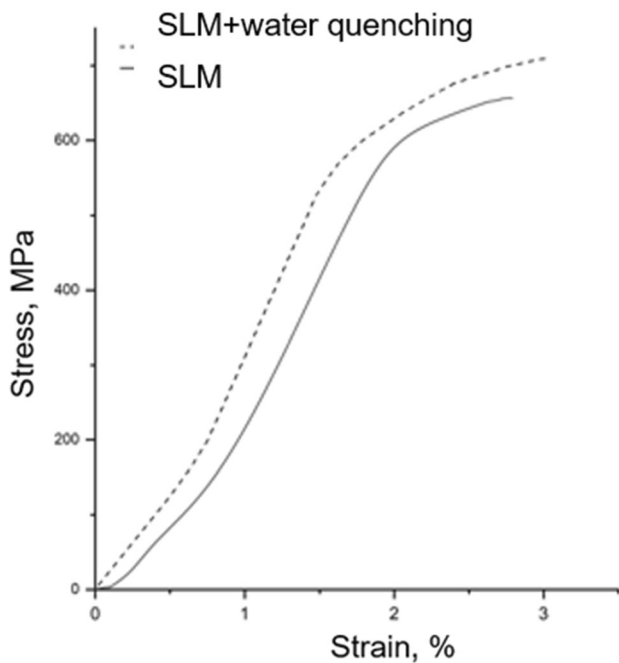


Fig. 9 Compressive stress–strain curves for $\text{Ti}_{25}\text{Zr}_{25}\text{Ni}_{25}\text{Cu}_{15}\text{Co}_{10}$ sample produced by PBF-LB at MV1 double mode before and after quenching

is shown. The optimal mode is determined to obtain samples without visible defects, with a porosity of less than 1%. It has parameters as followed:

Scanning of the sample “body”: laser power – 288 W, scanning speed 800 mm/s, layer thickness – 60 μm , number of scanning repetitions – 2, volume energy density – 120 J/mm^3 ;

Scanning the sample contour: laser power – 350 W, scanning speed 800 mm/s, layer thickness – 60 μm , number of scanning repetitions – 3, volume energy density – 145 J/mm^3 .

During PBF-LB of the HEA powders, a mixed structure is formed, consisting of grains of B2-TiNi-austenite (average size $\sim 5 \mu\text{m}$) with Laves phases and zirconium oxides.

The hardness of $\text{Ti}_{25}\text{Zr}_{25}\text{Ni}_{25}\text{Co}_{10}\text{Cu}_{15}$ alloy after PBF-LB is more than 600 HV that significantly exceeds the values obtained after conventional technologies.

According to the compressive ultimate strength, 640 MPa, and the compressive yield strength, 600 MPa, the synthesized samples are significantly inferior to those produced by conventional smelting technologies. However, the plasticity of 1.3% is comparable to that of the conventional alloys and indicates the prospects of using PBF-LB to obtain the Ti–Zr–Ni–Co–Cu HEAs.

Supplementary Information The online version contains supplementary material available at <https://doi.org/10.1007/s12666-022-02616-3>.

Acknowledgements This research was carried out with the support of the State contract # H.4M.241.09.20.1081 dated June 4, 2020 “Development and material science substantiation of the design of materials and products based on shape memory alloys with a controlled structure and piezoelectric ceramics using additive 4D technologies. Stage of 2020” (IGK 17706413348200001110).

References

- Cantor B, Chang I T H, Knight P, and Vincent A J B, *Mater Sci Eng A* **375–377** (2004) 213. <https://doi.org/10.1016/j.msea.2003.10.257>.
- Yeh J W, Chen S K, Lin S J, Gan J Y, Chin T S, Shun T T, Tsau C H, and Chang S Y, *Adv Eng Mater* **6** (2004) 299. <https://doi.org/10.1002/adem.200300567>.
- Miracle D B, Miller J D, Senkov O N, Woodward C, Uchic M D, and Tiley J, *Entropy* **16** (2014) 494. <https://doi.org/10.3390/e16010494>.
- Praveen S, and Kim H S, *Adv Eng Mater* **20** (2018) 1. <https://doi.org/10.1002/adem.201700645>.
- Lee J I, Tsuchiya K, Tasaki W, Oh H S, Sawaguchi T, Murakami H, Hiroto T, Matsushita Y, and Park E S, *Sci Rep* **9** (2019) 1. <https://doi.org/10.1038/s41598-019-49529-8>.
- Firstov G, Koval Y, van Humbeeck J, Timoshevskii A, Kosorukova T, and Verhovlyuk P, *Mater Sci Found* **81–82** (2015) 207. <https://doi.org/10.4028/www.scientific.net/msfo.81-82.207>.
- Chen C-H, and Chen Y-J, *Scr Mater* **162** (2019) 185. <https://doi.org/10.1016/j.scriptamat.2018.11.023>.
- Chen C H, Chen Y J, and Shen J J, *Met Mater Int* **50** (2019) 617. <https://doi.org/10.1007/s12540-019-00383-3>.
- Aksoy C B, Canadinc D, and Yagci M B, *Mater Chem Phys* **236** (2019) 121802. <https://doi.org/10.1016/j.matchemphys.2019.121802>.
- Hong S H, Kim J T, Park H J, Kim Y S, Suh J Y, Na Y S, Lim K R, Shim C H, Park J M, and Kim K B, *J Alloys Compd* **692** (2017) 77. <https://doi.org/10.1016/j.jallcom.2016.09.023>.
- Firstov G S, *Visn Nac Acad Nauk Ukraini* **06** (2018) 19. <https://doi.org/10.15407/visn2018.06.019>.
- Ntouanoglou K, Stavropoulos P, and Mourtzis D, *Procedia Manuf* **18** (2018) 120. <https://doi.org/10.1016/j.promfg.2018.11.016>.
- Farber E, Zhu J N, Popovich A, and Popovich V, *Mater Today Proc* **30** (2019) 761. <https://doi.org/10.1016/j.matpr.2020.01.563>.
- Yamamoto T, Kato H, Murakami Y, Kimura H, and Inoue A, *Acta Mater* **56** (2008) 5927. <https://doi.org/10.1016/j.actamat.2008.08.003>.
- Kim A, Makhmutov T, Razumov N, Silin A, Popovich A, Zhu J N, and Popovich V, *Mater Today Proc* **30** (2019) 679. <https://doi.org/10.1016/j.matpr.2020.01.521>.
- Makhmutov T, Razumov N, Kim A, Ozerskoy A, Mazeeva A, and Popovich A, *Met Mater Int* **27** (2020) 50. <https://doi.org/10.1007/s12540-020-00747-0>.
- Saedi S, Moghaddam N S, Amerinatanzi A, Elahinia M, and Karaca H E, *Acta Mater* **144** (2018) 552. <https://doi.org/10.1016/j.actamat.2017.10.072>.
- Chen G, Zhao S Y, Tan P, Yin J, Zhou Q, Ge Y, Li Z F, Wang J, Tang H P, and Cao P, *Trans Nonferrous Met Soc China (English Ed)* **27** (2017) 2647. [https://doi.org/10.1016/S1003-6326\(17\)60293-0](https://doi.org/10.1016/S1003-6326(17)60293-0).

19. Kim Y-W, Chung Y-S, Choi E-S, Nam T-H, and Im Y-M, *J Korea Foundry Soc* **31** (2011) 26. <https://doi.org/10.7777/jkfs.2011.31.1.026>.
20. Razumov N G, Makhmutov T Y, Kim A, Goncharov I S, Ozerskoi N E, Silin A O, and Mazeeva A K, and Popovich AA, *Metallogr Microstruct Anal* **10** (2021) 474. <https://doi.org/10.1007/s13632-021-00770-6>.
21. Persson K, *TiNi mp-571* (2016). <https://doi.org/10.17188/1276044>.

Publisher's Note Springer Nature remains neutral with regard to jurisdictional claims in published maps and institutional affiliations.